Advanced Robotics, 2013
Vol. 27, No. 8, 627–639, http://dx.doi.org/10.1080/01691864.2013.763752

Taylor & Francis
Taylor & Francis Group

FULL PAPER

Exploiting wheel slips of mobile robots to improve navigation performance

Naim Sidek[a]* and Nilanjan Sarkar[b]

[a]*Faculty of Engineering, Department of Mechatronics Engineering, International Islamic University Malaysia, PO Box 10, 50728 Kuala Lumpur, Malaysia;* [b]*Department of Mechanical Engineering, Vanderbilt University, VU Station B 351592, 2301 Vanderbilt Place, Nashville, TN 37235-1592, USA*

(*Received 3 April 2013; accepted 17 July 2012*)

Improving navigation performance of autonomous wheeled mobile robot (WMR) in a dynamic unstructured environment requires improved maneuverability. In such cases, the dynamics of wheel slip may violate the ideal no-slip kinematic constraints generally used to model nonholonomic WMR. In this paper, a new method is proposed to tackle the modeling inadequacy that arises when slip is neglected by including both longitudinal and lateral slip dynamics into the overall dynamics of the WMR. This new model of the WMR provides a realistic simulation environment that can be utilized to develop model-based controllers to improve WMR navigation. In this paper, a dynamic planner with a path-following controller is designed to allow the WMR to navigate efficiently by autonomously regulating the generated traction force due to wheel slip. Extensive simulation results demonstrate the importance of the proposed modeling technique to capture slip phenomenon and the efficacy of the presented control technique to exploit such slip for better navigation performance.

Keywords: nonholonomic wheeled mobile robot; wheel slip; path-following control; traction circle

1. Introduction

The application of wheeled mobile robots (WMRs) has been rapidly increasing in recent years. While the overall capabilities of the WMRs have improved significantly over the years, the ability of the WMR to operate autonomously at a high speed on unstructured environment remains as a challenge. We argue that wheel slip is an important factor that can impact WMR navigation in such applications (e.g. target chasing, dynamic obstacle avoidance etc.) and can effectively be exploited to improve maneuverability. However, any planner and controller that need to be developed to meet this challenge must be extensively investigated in simulation environment before they can be applied to real robots to minimize both risk and cost factors. In recent years, researchers have developed sophisticated simulation environment for WMR, such as *Player/Stage* and *Microsoft Robotics Studio*, that provide realistic modeling platforms to develop planning and control methodologies for WMRs. While these platforms have become quite useful for general WMR applications, they do not provide mechanisms to model wheel slip and, thus, may not be as effective in applications where slip is a significant factor. Instead, these simulation platforms offer high-level planning strategies to offset the effect of slip when the WMR is deployed in real-world environment.[1] One of the problems of this approach is that one cannot fully exploit the capabilities of model-based control approach, which is the predominant control strategies in WMR literature, since the model does not capture the slip phenomenon. In order to clarify this point, let us consider Figure 1. In Figure 1(a), we present the tracking performance of a proportional-integral-derivative navigation controller in negotiating right-angled path in *MobileSim* simulation environment for a Pioneer P3DX robot. Since the tracking is acceptable in the simulation environment, we use the same controller with the same gains to replicate the tracking performance in the real environment, as shown in Figure 1(b) and (c). When the wheel slip is not large (Figure 1(b)), the tracking performance reasonably mirrors simulation results. However, when the wheel slip is large (Figure 1(c)) (i.e. when we made the floor slippery), the navigation performance of the same controller becomes unacceptable (i.e. the WMR deviates more than 90° from the desired path). Ideally, a well-designed controller should be able to rectify the error in path following, possibly by autonomously reducing the desired forward velocity, such that the WMR stays on the path.

*Corresponding author. Email: snaim@iium.edu.my

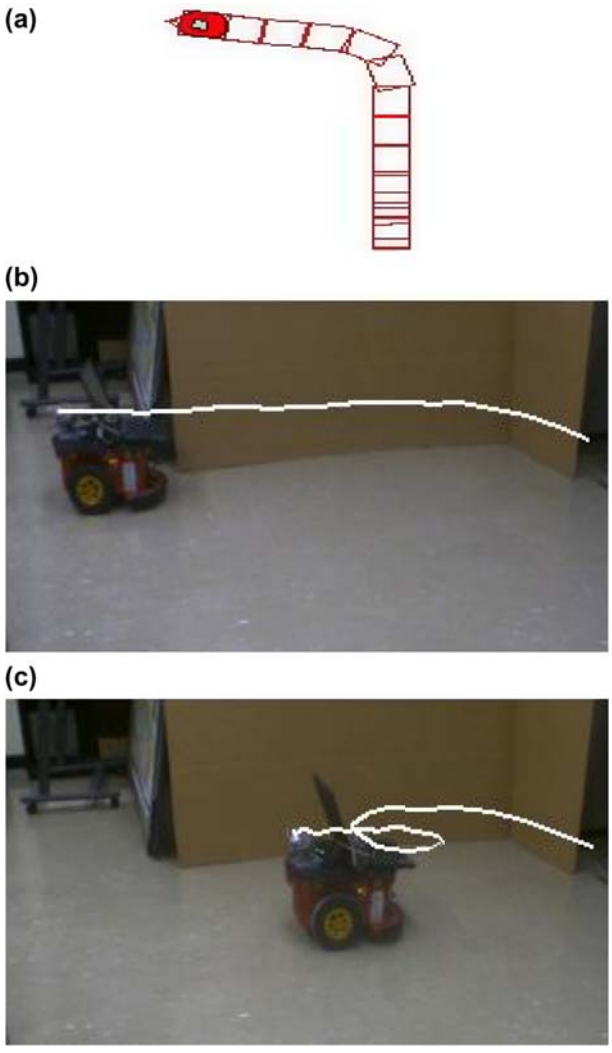

Figure 1. Robot path following (a) simulation (from top view) showing (b) small slip, and (c) large slip.

Since the simulation environment does not model slip, it negates the benefit of the effort spent in developing the controller in the simulation environment, as seen in Figure 1(c).

We, therefore, argue in this paper that it is important to explicitly model slip within the WMR dynamics and utilize such models to develop model-based control strategies for WMR navigation. A review of WMR literature indicates that conventional modeling of a WMR assumes nonholonomic no-slip constraints at the contact point between a wheel and the ground surface.[2–6] These constraints are developed based on the ideal case where the longitudinal motion of the wheel is pure rolling and, as such, the longitudinal slip at the contact point between the wheel and the surface is always zero. The lateral slip at the contact point is also assumed to be zero. Such assumptions are acceptable if the WMR moves slowly, on a regular surface where slip is negligible. However, when the WMR moves at a high speed on an irregular surface (e.g. a slippery surface) such no-slip assumptions cannot be justified. It is important to understand how slip impacts WMR navigation by developing system models that allow systematic investigation of wheel slip. There are a few recent papers that present approaches to model wheel slips. Motte and Campion [7] is one of the earliest papers which considers slip in the WMR dynamic model. The authors modeled the slip as a small constraint violation covering the linear part of the traction curve. Lin et al. [8] represented a novel way to model the constraint violation due to wheel slip using an anti-slip factor. By using anti-slip control, the simulation results promised stability for the desired robot trajectory. Tarokh, McDermott and Volpe [9,10] introduced the slip states into a generalized WMR kinematic model. Dixon [11] treated slip as a small, measureable, bounded perturbation in the WMR kinematic model. Ramakrishna and Ghosal [12] indirectly included traction force in the system model by measuring the magnitude of slip. However, the slip was assumed to be very small, thus, was omitted in the system dynamic equation. Jung, Hsia and Stonier [13,14] applied similar concept but specific to lateral traction on a bicycle model and on an omni-directional WMR, respectively. Small slip angle was found to be proportional to lateral traction force and was embedded in the dynamics of skid steer WMR as reported in [15]. However, the model did not address the large slip angle. Lin et al. [8] introduced the notion of slip space to analyze the dynamics of slip of an omni-directional WMR and Graciam and Tornero [16] proposed slip model based on successive approximation of WMR dynamics which is based on industrial forklift.

In this paper, as our first contribution, we present a general dynamic modeling approach that can model both longitudinal and lateral wheel slips which utilizes the overall range of slip–traction relationship within the original dynamics of the WMR. We argue that the inclusion of the slip dynamics into the overall dynamics of the WMR will allow the development of advanced planning and control mechanisms that can take advantage of the slip phenomenon instead of trying to neglect or suppress it.[7,17,18] In particular, as our second contribution of this paper, we design a dynamic planner and a path-following controller that can ensure the navigation stability when the WMR is subjected to both longitudinal and lateral slips. The paper is organized as follows: in Section 2, a new, generalized dynamic modeling technique of the WMR is developed. This is followed by a discussion on the design of the dynamic path-following controller in Section 3. Simulation results are presented in Section 4 to demonstrate the efficacy of our proposed modeling and control technique for surfaces with different friction coefficients. Section 5 presents the conclusion of this paper as well as the direction of future works.

2. Modeling framework

2.1. Dynamic model of a general nonholonomic WMR

In this paper, we adopt the *Lagrangian* formalism to derive the dynamic equation of a WMR. While the parts of the following formulation are not new and were previously explored by several researchers,[7,14,19–22] we present this formulation since it is needed to combine the slip dynamics with that of the WMR. When the WMR is subjected to the nonholonomic kinematic constraints on a planar surface, the equation of motion can be written in the following generalized form:

$$M(q)\ddot{q} + C(q,\dot{q}) = B(q)u + A^T(q)\sigma \tag{1}$$

where $q \in \Re^{n\times 1}$ is a vector of generalized coordinates and $\dot{q} \in \Re^{n\times 1}$ is a vector of linear and angular velocities of generalized coordinates. $M(q) \in \Re^{n\times n}$ is a symmetric positive definite inertia matrix of the system. $C(q,\dot{q}) \in \Re^{n\times 1}$ is the centrifugal and Coriolis forces vector. $B(q) \in \Re^{n\times(n-m)}$ and $u \in \Re^{(n-m)\times 1}$ are the input transformation matrix and input vector, respectively. $\sigma \in \Re^{m\times 1}$ is a vector of *Lagrange* multipliers and $A^T\sigma$ corresponds to the generalized forces related to the kinematic constraints. The constraint equations can be defined as:

$$A(q)\dot{q} = 0 \tag{2}$$

$A(q) \in \Re^{m\times n}$ is a matrix associated with the kinematic constraints of the nonholonomic system.

For the WMR shown in Figure 2, the generalized system coordinates are given as:

$$q = [x_c, y_c, \phi, \theta_1, \theta_2, \theta_3, ..., \theta_{n-1}, \theta_n]^T \tag{3}$$

where (x_c, y_c) is the coordinate of the reference point on the WMR platform, ϕ is the platform orientation with respect to an inertial frame $\{x_I, y_I\}$, and $\theta_i, i = 1, 2, \ldots, n$ are the wheel angular displacements. In many conventional systems, the constraint equations in Equation (2) are defined under the assumption that the wheels roll without longitudinal slip and there is no lateral slip.

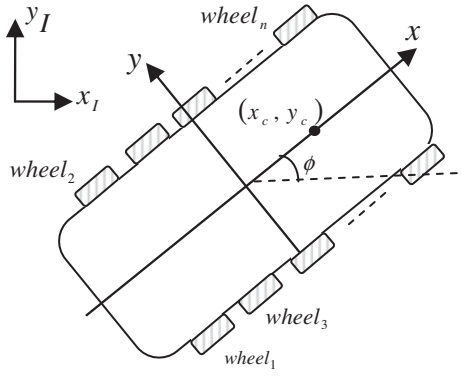

Figure 2. Generalized nonholonomic WMR platform.

Hence, if slip occurs, these assumptions are clearly violated. *In this paper, we argue that the modeling of the WMR that is based on the assumption of wheel pure rolling and zero lateral slipping (for WMR with unicycle type of wheel) in a real practical situation is rather unrealistic. Our solution it to relax the assumptions by introducing new state due to wheel slips.* As shown in Figure 3, we introduce ζ_i and η_i to represent the longitudinal slip and the lateral slip displacements when the wheel is rolling from time t to $t + \Delta t$, for the ith wheel of the WMR, respectively. The wheels are rigidly connected to the WMR's body, as shown in Figure 2. Hence, we can write slip coordinates in the following vector form:

$$q_2 = [\eta_1, \zeta_1, \eta_2, \zeta_2, ..., \eta_n, \zeta_n]^T \tag{4}$$

In order to include the slip dynamics into the overall dynamics of the WMR, let us rename the original set of generalized coordinates, q in Equation (3) as q_1. We then augment the generalized coordinates q_1 by including the slip coordinates q_2 to form a new set of generalized coordinates as follows:

$$q = [q_1^T \; q_2^T]^T \tag{5}$$

The new coordinate system allows us to describe the motion of the system in the presence of slip. We then define $S(q) \in \Re^{n\times(n-m)}$ to be a full rank matrix formed by a set of smooth and linearly independent vector fields, spanning the null space of $A(q)$. Thus, the result of multiplication of these matrices, $S(q)^T A(q)^T = 0$. It is then possible to find a set of vector of time functions,

$$v(t) \in \Re^{(n-m)\times 1}, \forall t \tag{6}$$

so as,

$$\dot{q}(t) = S(q)v(t) \tag{7}$$

We can use Equation (7) to eliminate the *Lagrange* multipliers in Equation (1). We further differentiate Equation (7), to get state acceleration as follows:

$$\ddot{q} = \dot{S}(q)v(t) + S(q)\dot{v}(t) \tag{8}$$

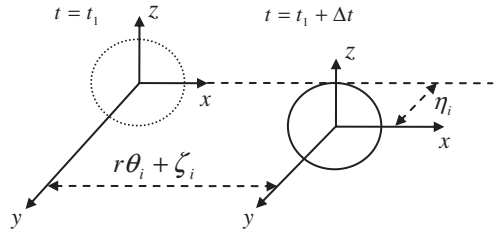

Figure 3. Wheel's rolling with both longitudinal and lateral slip displacements on planar surface.

By introducing Equations (7) and (8) into Equation (1), we get:

$$\dot{v}(t) = (S^T M S)^{-1} S^T (-M\dot{S}v - C - Bu) \tag{9}$$

where $\dot{v}(t)$ are the acceleration of vector time function defined in Equation (6). We can utilize Equation (9) to develop a suitable model-based controller.

2.2. Detailed modeling of a two-wheeled nonholonomic mobile robot with wheel slips

The WMR, shown in Figure 4, is a standard platform of a nonholonomic two-WMR. It has two unicycle driving wheels and a caster wheel. The driving wheels are powered by DC motors and have the same wheel radius, r. The center of mass (COM) is located at point P_c and P_l is defined as a look-ahead point located on the x-axis of the WMR body. Point P_o is the origin of WMR axis, which is located at the intersection of the longitudinal x-axis and the lateral y-axis. a is the length of the WMR body and b is the distance measured from the center of the robot body to the center of the wheel. d denotes the distance between point P_o and point P_c along the x-axis.

The origin of the inertial frame $\{X,Y\}$ is shown as P_I and as such allows the pose of the WMR to be completely specified through the following vector of generalized coordinates,

$$q = [x_c, y_c, \phi, \theta_1, \theta_2]^T \tag{10}$$

where x_c and y_c are the coordinates of the COM. φ represents the orientation of the WMR frame from the inertial frame and $[\theta_1, \theta_2]$ is the angular displacement vector for the WMR driving $wheel_1$ and $wheel_2$, respectively.

In this paper, we want to investigate the navigation problem of a nonholonomic WMR when the ideal no-slip assumption does not hold true, thus we start by

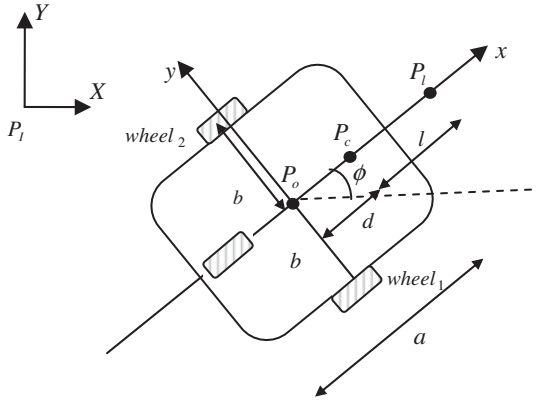

Figure 4. A two-wheeled nonholonomic mobile robot platform.

introducing the new slip coordinate vector, $q_2 = [\eta_1, \eta_2, \zeta_1, \zeta_2]^T$. This slip vector is composed of four components that represent longitudinal slip displacements ζ_1 and ζ_2, and lateral slip displacements η_1 and η_2 for $wheel_1$ and $wheel_2$, respectively. The slip vector can be easily expanded to accommodate a WMR with more wheels. We then augment the generalized coordinate vector in Equation (10) to include the slip vector to develop a new augmented vector of generalized coordinates as follows:

$$q = [x_c, y_c, \phi, \eta_1, \eta_2, \zeta_1, \zeta_2, \theta_1, \theta_2]^T \tag{11}$$

The new generalized coordinate vector, $q = [q^T_{1(1\times n)}\ q^T_{2(1\times s)}]^T$ spans the space $\Re^{n+s}$, where $q_{1(5\times 1)}$ is the original generalized vector and $q_{2(4\times 1)}$ is the slip vector. Using the new generalized vector, we can formulate the rolling constraints of the WMR with two fixed driving wheels in the following form:

$$\begin{aligned} r\dot{\theta}_1 + \dot{\zeta}_1 &= \dot{x}_c \cos\phi + \dot{y}_c \sin\phi + b\dot{\phi} \\ r\dot{\theta}_2 + \dot{\zeta}_2 &= \dot{x}_c \cos\phi + \dot{y}_c \sin\phi - b\dot{\phi} \end{aligned} \tag{12}$$

Equation (12) relaxes the assumption of no slipping by allowing the longitudinal velocity of the COM at point P_c to be a summation of the longitudinal velocity generated by the wheel angular velocity and the longitudinal slip velocity.

The same idea can be applied to develop the knife-edge/lateral constraints. Note that lateral slip in each wheel of a WMR is independent if the wheels are connected to the body of the WMR with mechanisms that allow relative motion (e.g. connected using springs and dampers). However, in our case, as shown in Figure 4, the two wheels of the WMR are rigidly connected to the body of the WMR and thus cannot have two different lateral slips as can be seen from the following equations where both $\dot{\eta}_1$ and $\dot{\eta}_2$ have the same expressions,

$$\begin{aligned} \dot{\eta}_1 &= \dot{y}_c \cos\phi - \dot{x}_c \sin\phi - d\dot{\phi} \\ \dot{\eta}_2 &= \dot{y}_c \cos\phi - \dot{x}_c \sin\phi - d\dot{\phi} \end{aligned} \tag{13}$$

where lateral slip is allowed to occur along the turning axis of the WMR during cornering. In this paper, we analyze the effect of both slips, particularly, to investigate the agility of WMR navigation to negotiate sharp cornering. Now, after we rearrange the coordinate system, the new constraints defined above can be

rewritten in the form of Equation (2). We find this matrix to be a full rank matrix. We then construct matrix $S(q) \in \Re^{9\times 5}$ and choose an auxiliary vector time function of $v(t) \in \Re^{5\times 1}$. We select the function that has direct relationship to the generalized force as:

$$v = [\dot{\eta}_2, \dot{\zeta}_1, \dot{\zeta}_2, \dot{\theta}_1, \dot{\theta}_2]^T \tag{14}$$

In order to formulate the inertia matrix, we define the kinetic energy of the WMR as follows:

$$\begin{aligned} T_r &= \frac{1}{2}m_r(\dot{x}^2 + \dot{y}^2) + \frac{1}{2}I_{rz}\dot{\phi}^2 \\ T_{w1} &= \frac{1}{2}m_w(r\dot{\theta}_1 + \dot{\zeta}_1)^2 + \frac{1}{2}m_w\dot{\eta}_1^2 + \frac{1}{2}I_{wz}\dot{\phi}^2 + \frac{1}{2}I_{wy}\dot{\theta}_1^2 \\ T_{w2} &= \frac{1}{2}m_w(r\dot{\theta}_2 + \dot{\zeta}_2)^2 + \frac{1}{2}m_w\dot{\eta}_2^2 + \frac{1}{2}I_{wz}\dot{\phi}^2 + \frac{1}{2}I_{wy}\dot{\theta}_2^2 \end{aligned} \tag{15}$$

where T_r is the kinetic energy of the WMR body and, T_{w1} and T_{w2} are the kinetic energies for $wheel_1$ and $wheel_2$, respectively. Note that the terms in Equation (15) associated to the slip variables are, in essence, the work done by the longitudinal and the lateral friction forces. Next, we introduce a vector of lateral and longitudinal traction force,

$$F(\dot{q}) = [0, 0, 0, f_{lat\ 1}, f_{lat\ 2}, f_{longid\ \ 1}, f_{longid\ \ 2}, 0, 0]^T. \tag{16}$$

Each individual value of the traction force vector is calculated from the magnitude of the respective slips based on the concept of traction circle. Now, the dynamics of the WMR can be written as a coupled nonlinear system, $\dot{v} = \lambda + \kappa\tau$ (i.e. Equation (9)) where,

$$\begin{aligned} \lambda &= (S^T M S)^{-1} S^T (-M\dot{S}v - F) \\ \kappa &= (S^T M S)^{-1} S^T B \end{aligned} \tag{17}$$

2.3. Traction force model

In this paper, we investigate the effect of both longitudinal traction force during acceleration and deceleration and lateral traction force during turning on the WMR navigation. The value of longitudinal traction force, f_{longid_i}, varies based on the magnitude of slip ratio,

$$sr_i = \frac{r\dot{\theta}_i - V}{abs(r\dot{\theta}_i)} = \frac{\dot{\zeta}_i}{abs(r\dot{\theta}_i)} \tag{18a}$$

Meanwhile, the function of lateral traction force, f_{lat_i} takes slip angle, *sa*, as its main input. Slip angle is defined as the angle between the instantaneous velocity of the WMR and the instantaneous linear velocity of the wheel. This angle is the result of the lateral slip and is defined as follows:

$$sa_i = \tan^{-1}\left(\frac{\dot{\eta}_i}{abs(r\dot{\theta}_i)}\right) \tag{18b}$$

An elegant, semi-empirical model based on curve fitting, called *Pacejka* model or *Magic formula*, has been widely accepted in industry and academia[23] to generalize the model of traction force vs. tire slip. The equation is written in the following form:

$$F = K_1 \sin(K_2 \tan^{-1}(SK_3 + K_4(\tan^{-1}(SK_3) - SK_3))) + S_v \tag{19}$$

where S is a function of slip angle or slip ratio for lateral and longitudinal tractions, respectively. All the variables, $K_i,\ i = 1, \ldots, 4$ and S_v, are constants and determined from the curve fitting process of the empirical data and can also be related to the tire characteristics. There are several ways to combine the formula for longitudinal and the lateral tractions together as reported in [24]. In this paper, we apply the concept of traction circle to measure the combined traction force.

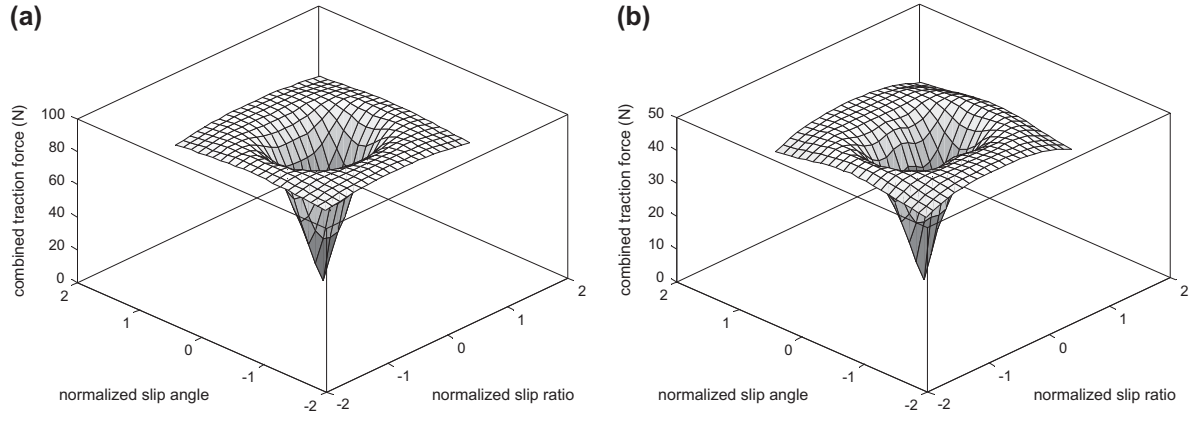

Figure 5. Traction force vs. slip-angle/slip ratio relationship for two surfaces with different friction coefficients (a) 1.0 and b(b) 0.5.

In Figure 5, we illustrate two examples of combined traction forces developed using Equation (19) on surfaces that have the coefficients of friction of 1.0 (Figure 5 (a)) and of 0.5 (Figure 5(b)). It can be seen from these figures that the magnitude of traction force varies with the slip quantities. The traction force has its maximum all the way around the traction circle. The region in the 'cup' (i.e. from the origin to the circular peak of the curve) represents a stable region. Once the slip quantities exceed the peak values, the traction force begins to decrease gradually and thus the region outside the 'cup' is known as unstable region. When entering this region from a stable 'cup' region, the loss of grip of the tire on the surface is sudden and may send the WMR out of control. It is our objective to optimize the control objectives while staying in the stable region.

3. Control and navigation

We now present the design of a path-following controller that allows the WMR to navigate in the presence of slip. The goal here is to ensure that the WMR can follow a specific path with a desired forward velocity while negotiating slip. However, if the WMR determines that it is becoming unstable while trying to achieve the desired velocity due to slip, then it will autonomously reduce the forward velocity exploiting the maximum allowable traction forces from the slip–traction properties to follow the path under the given condition. In this paper, by navigation performance, we mean the ability of the WMR to follow a given path with a given forward velocity. However, between these two tasks, we assign a higher priority on staying on the path over achieving the desired forward velocity if wheel slip causes instability.

3.1. Output equations and feedback linearization

In this work, based on the dynamic model previously developed, we approach the problem of WMR navigation under the path-following formulation. Referring to Figure 4, the coordinates of the look-ahead point P_l are given by:

$$\begin{aligned} x_l &= x_c + l\cos\phi \\ y_l &= y_c + l\sin\phi \end{aligned} \tag{20}$$

By following the conventional wisdom in which one drives a car, we can establish the following two driving objectives:

(1) The WMR has to pursue a given prescribed path as closely as possible, and
(2) The WMR has to travel the path with a given desired forward velocity.

Based on the above objectives, we can establish the output equations where the first equation relates the shortest distance between the WMR (a reference point on the WMR platform) and the desired path. The second equation is to describe the WMR forward velocity. Let the output equation be represented by a vector y, where,

$$y = h = [\,h_1(q) \quad h_2(v)\,] \tag{21}$$

where $h_1(q)$ is a measure of the first objective and $h_2(v)$ is a measure of the second objective.

Since any set of paths can be constructed through a combination of circular path segment and straight line path segment,[10] we develop explicit equations for $h_1(q)$ for both circular and straight line paths. For a circular path, $h_1(q)$ can be formulated as follows:

$$\begin{aligned} h_1(q) &= h_1(x_c, y_c, \phi) \\ &= \sqrt{((x_l - x_f)^2 + (y_l - y_f)^2)} - R \end{aligned} \tag{22}$$

$P_f = (x_f, y_f)$ is the instantaneous center of circular path with respect to an inertial frame and R is the instantaneous radius of the circular path. Points $P_l = (x_l, y_l)$ (the look-ahead point) and $P_c = (x_c, y_c)$ (the COM) are related through Equation (22).

As for a straight line path, the output equation becomes:

$$h_1(x_c, y_c, \phi) = \frac{C_1 x_l + C_2 y_l + C_3}{\sqrt{C_1^2 + C_2^2}} \tag{23}$$

where all C_i, $i = 1, 2, 3$ are constants used to describe the straight line. From Equations (22) and (23), we see the shortest distance between the look-ahead point and the path can be taken as the absolute value of h_1. After the introduction of longitudinal slip, the forward velocity of the WMR can be written as follows:

$$\begin{aligned} h_2(v) &= \dot{x}_c\cos\phi + \dot{y}_c\sin\phi \\ &= \frac{(r\dot{\theta}_1 + \dot{\zeta}_1) + (r\dot{\theta}_2 + \dot{\zeta}_2)}{2} \end{aligned} \tag{24}$$

where $\dot{\theta}_1$, $\dot{\theta}_2$, $\dot{\zeta}_1$, and $\dot{\zeta}_2$ are v_2, v_3,, v_4, and v_5, respectively.

Now, we proceed to develop a nonlinear controller based on the feedback linearization technique. The decoupling matrix for feedback linearization for the above output equations is derived as follows:

$$\ddot{y}_1 = \frac{\partial(J_{h_1}S(q))}{\partial q}\dot{q}v + J_{h_1}(q)S(q)\dot{v}$$

$$\dot{y}_2 = J_{h_2}\dot{v} \tag{25}$$

and we can set $\dot{v} = u$ where u is the new input to the control system.

$J_{h_i} = \frac{\partial h_i}{\partial q}$ is known as *Jacobian* matrix and we can use them to compute the decoupling matrix, Φ as follows:

$$\Phi = \begin{bmatrix} J_{h_1}(q)S(q) \\ J_{h_2} \end{bmatrix} \tag{26}$$

We utilize the decoupling matrix to establish the input-output feedback linearization as shown below:

$$\ddot{y} = \begin{bmatrix} \ddot{y}_1 \\ \dot{y}_2 \end{bmatrix} = \dot{\Phi} \begin{bmatrix} v \\ 0 \end{bmatrix} + \Phi u \tag{27}$$

If we let $u = \dot{v}$ and represent Equation (28) in the form of $\ddot{y} = U + V\dot{v}$, with Equation (17) we can write $\ddot{y}$ in the following form:

$$\ddot{y} = U + V\lambda + W\tau \tag{28}$$

where $W = V\kappa$. The relationship between torque and traction force can then be determined directly from the inverse dynamic relationship as given:

$$\tau = W^{-1}(u_d - U - V\lambda) \tag{29}$$

where W^{-1} is taken to be the inverse of W. If we let error, $e = h_{i\_desired} - h_{i\_actual}$, then the desired control u_d can be computed as follows:

$$u = \ddot{y}_{desired} + K_v\dot{e} + K_p e \tag{30}$$

where K_v and K_p are constant gains for the linear outer feedback loop chosen to ensure the convergence of the control error.

3.2. Dynamic planner

In order to implement the dynamic planner with the path-following controller, which is subjected to wheel slip, we model the desired control input using a function of traction force as follows:

$$J(F) = \frac{F_{\max}F}{abs(F_{\max} - F)^{\mu}} \tag{31}$$

where μ is the decay factor and $f_{\max}$ is the peak traction force and is dependent on the type of ground surfaces. F is instantaneous traction force related to Equation (19). Now we define,

$$K(F) = \frac{1}{1 + abs(J(F))} \tag{32}$$

which behaves as a weighted coefficient to the desired forward velocity. From Equation (32), we notice that the weight approaches the value of 1.0 as the traction force gradually moves away from the prespecified allowable maximum traction, $F_{\max}$. It converges to zero as it approaches $F_{\max}$. The rate of convergence can be set by using the decay factor, μ. For such a WMR that can reach a maximum velocity of $V_{\max}$, we could set our desired forward velocity to be:

$$h_{2desired} = K(F)V_{\max} \tag{33}$$

and the desired absolute distance to be within a predefined boundary,

$$h_{1desired} = \text{absolute distance} < |\varepsilon| \tag{34}$$

where ε can be taken as a small number.

The above dynamic planner essentially regulates the desired forward velocity that is provided to the path-following controller as a reference input based on slip–traction relationship. In other words, it indirectly limits the slip such that the WMR can operate within the maximum allowable traction force.

4. Results and discussion

We first present simulation results to demonstrate the validity of the WMR model that include slip dynamics and the efficacy of the dynamic path-following controller that utilizes slip–traction properties. We also present preliminary experimental results to show the effectiveness of the developed simulation environment in analyzing and translating the simulation results in experiments. For the simulation task, we chose the WMR parameters (refer Figure 4) as follows: $b = 0.24$ m; $d = 0.05$ m; $r = 0.095$ m; $m_r = 16$ kg; $m_w = 0.5$ kg; $I_{rz} = 0.537$ kg m^2 (i.e. assuming solid cuboid); $I_{wy} = 0.0023$ kg m^2; $I_{wz} = 0.0011$ kg m^2 (i.e. assuming thin solid disk). The look-ahead point is at 0.5 m away from point P_c along the x-axis of the WMR body. The gains for the linear feedback loop are designed in such a way that we can get a critically damped output response where $K_{p1} = 400$, $K_{v1} = 100$ and $K_{v2} = 10$. The decay factor, μ in Equation (35), regulates traction performance. In this simulation, we choose $\mu = 2.5$. We apply our proposed approach to the WMR navigation that is subjected to both lateral and longitudinal slips. As for the desired path the WMR has to follow, it is composed of two straight line segments (i.e. segment AB and segment BC), connected at a right angle to resemble a sharp corner. The idea to have such a shape of path is to observe the effect of slip when the WMR needs to navigate through sharp cornering, simulating a harsh yet realistic navigation scenario (e.g. in target chasing scenario or in avoiding dynamic obstacles

etc.). Additionally, we are interested in investigating how the presented controller allows autonomous navigation on different surfaces having varying traction properties. Therefore, we conduct simulation studies to show how the WMR performs during cornering on two different surfaces under three different scenarios (i.e. *Case I, II*, and *III*). For the first two cases, we specify a fixed reference velocity for the WMR and let the controller Equation (30) attempt to achieve this velocity on both surfaces. Here, we do not let the dynamic planner Equation (32) play any role so that we can observe the navigation performance of the WMR under different velocities without any dynamic adjustment of the reference input (i.e. the forward velocity). As we will see, navigation performance depends on the desired velocity, which varies for different surfaces. Then, in Case III, we demonstrate how the navigation performance can be improved by the introduction of the dynamic planner in conjunction with the controller such that the WMR can autonomously adjust its velocity to avoid excessive slipping leading to instability. The WMR autonomously adjusts its desired forward velocity based on the algorithm in the dynamic planner as discussed under the section 'Dynamic Velocity Planner.' From Equation (32), the weighted coefficient is used to regulate the desired forward velocity. For example, when the WMR is at zero velocity, the lateral traction force is zero. This set $J(F) = 0$ and $K(F) = 1$, and the desired forward velocity becomes the maximum allowable forward velocity. If the WMR is at the maximum allowable traction, $J(F)$ becomes infinity and $K(F) = 0$. This signals the robot to reduce its current forward velocity. The rate of regulation of forward velocity can be controlled by setting the decay factor, μ accordingly. For each of these cases, we set the initial states in such a way that the WMR can reach the desired forward velocity before encountering the first turn. The two surfaces that we use in this analysis are characterized by two different values of friction coefficients. The Surface 1 has a coefficient of friction of 1.0 represents a dry asphalt surface.[25,26] The Surface 2, on the other hand, has a coefficient of friction of 0.5 which represents a loose gravel surface.[25,26] Figure 5 (a) and (b) shows the traction circle properties for the above-mentioned two surfaces. The maximum allowable torque for each driving motor is set to 5.24 N-m and the absolute distance ε, in Equation (31) is set to be zero.

Case I: Effect of longitudinal and lateral slips on navigation performance on both Surface 1 and Surface 2 when the desired forward velocity is 2 m/s.

The WMR navigates on both surfaces in a stable manner, as shown in Figure 6. However, note that (refer inset of Figure 6) the WMR deviates from the desired path more on Surface 2 due to slip, which resulted in a longer time to reach the desired destination at $y = 5$ (i.e. it took 0.1262 s longer for Surface 2).

From Figure 7, we observe that the WMR reaches the desired forward velocity faster on Surface 1 than on Surface 2. This happens due to larger longitudinal wheel slip on Surface 2 at the beginning of the navigation (segment AB in Figure 8) in order to generate enough traction to propel the WMR forwards. As expected, there is no lateral slip on either surface on segment AB (Figure 9). However, as the WMR begins turning, the wheels start slipping laterally (Figure 9, segment BC). Note that a larger magnitude of lateral slip occurs on Surface 2 in order to generate the required traction force to balance the lateral momentum of the WMR. Similarly, a relatively larger magnitude of longitudinal slip is observed on Surface 2 as compared to Surface 1 (Figure 8, segment BC).

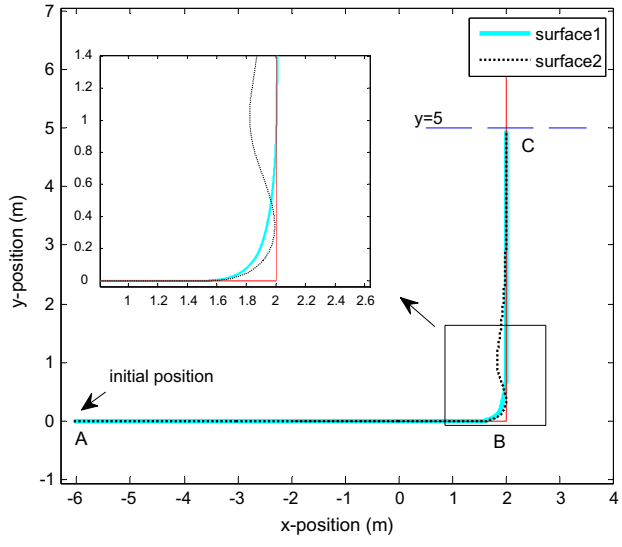

Figure 6. WMR's path-following trajectory.

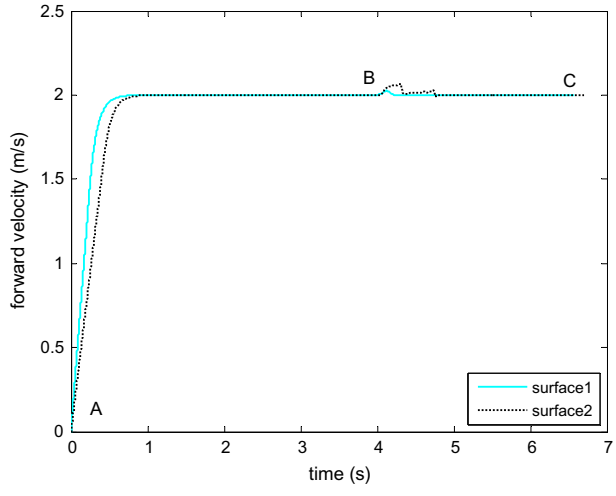

Figure 7. Forward velocity profile.

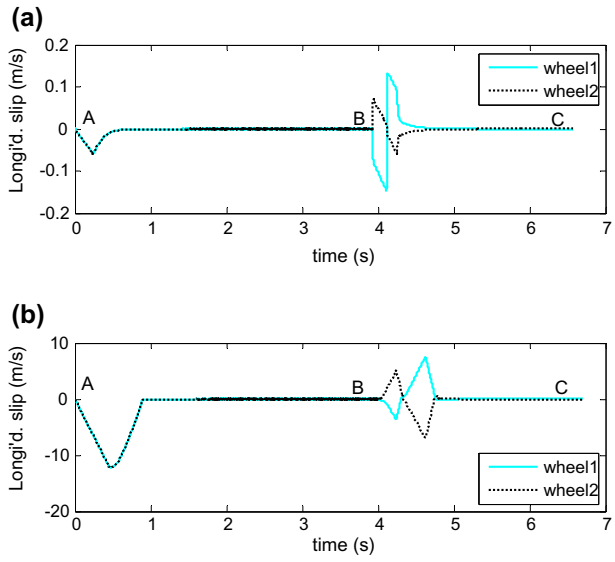

Figure 8. Longitudinal slip velocity on (a) Surface 1, (b) Surface 2.

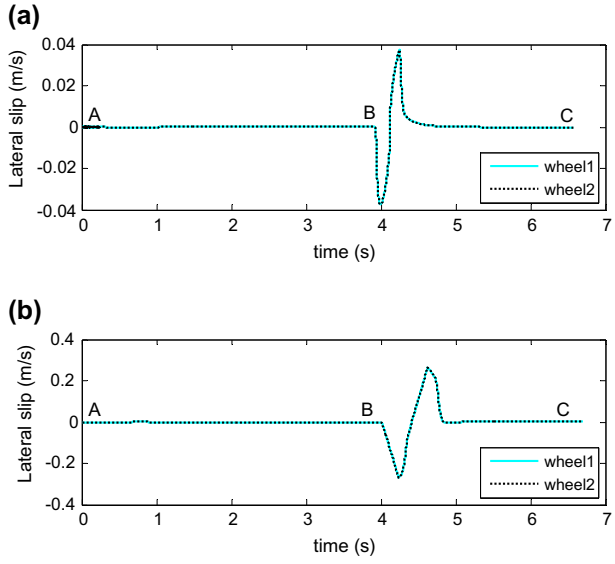

Figure 9. Lateral slip velocity on (a) Surface 1, (b) Surface 2.

We observe that slips on both surfaces reduce over time indicating that the WMR is capable of following the desired path at the desired forward velocity on both surfaces. This suggests the possibility of further increasing the desired forward velocity of the WMR for the given path, which we study in *Case II*.

Case II: Effect of longitudinal and lateral slips on navigation performance on both Surfaces 1 and 2 when the desired forward velocity is 3.2 m/s.

Now in *Case II*, we increase the desired forward velocity of the WMR navigation to 3.2 m/s. The objective is to investigate how slips on different surfaces influence WMR navigation as the forward velocity is increased. Such an investigation will provide insight on the maximum allowable forward velocity of a WMR for a given surface and will help develop advanced planners that can accommodate slip characteristics during path planning for an autonomous controller. As one would expect, and is shown in Figure 10, the WMR slips more at this forward velocity on both surfaces as compared to *Case I*. But more importantly, the slip on Surface 2 is so much that the WMR becomes unstable and deviates uncontrollably from the given path. Here, the WMR makes six attempts (as can be seen from six turning radii) to follow the path on Surface 2 before turning towards opposite direction. As can be seen from the slip–traction property (Figure 5(b)), excessive slip beyond the peak of the traction circle (which depends on the nature of the surface) reduces that available traction force and leads to instability. Thus, a controller with a fixed reference forward velocity and fixed gains may not be suitable in such a scenario. In order to address this issue, we propose a new dynamic planner that can modify the reference input as discussed in *Case III*.

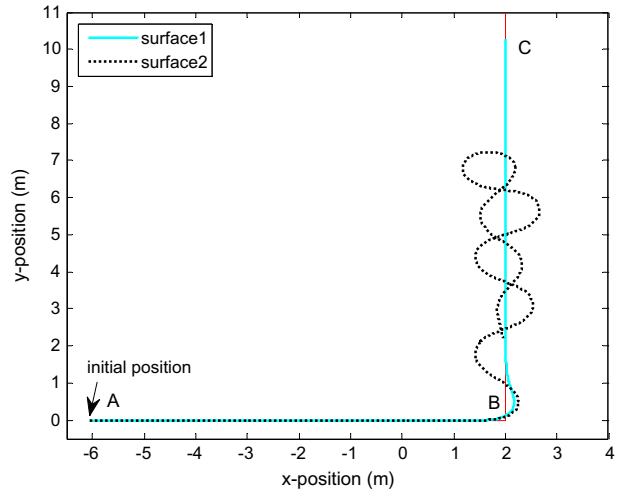

Figure 10. WMR's path-following trajectory.

From Figure 11, when we compare to *Case I,* we observe that the magnitude of the longitudinal slip is larger and it takes longer time to reduce (segment AB). On the second straight segment, BC, while the WMR can navigate on Surface 1 in a stable manner, the slip does not get reduced Surface 2. The navigation instability can also be seen on the lateral slip profile, as shown in Figure 12, as the magnitude of slip increases gradually over time.

Case III: Effect of a planning strategy to control the longitudinal and lateral slips on both Surface 1 and Surface 2 by autonomous adaptation of the desired forward velocity (max 3.2 m/s)

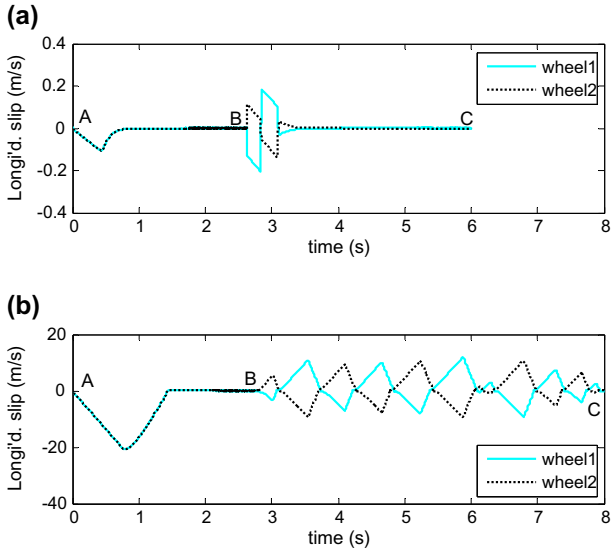

Figure 11. Longitudinal slip velocity on (a) Surface 1 and (b) Surface 2.

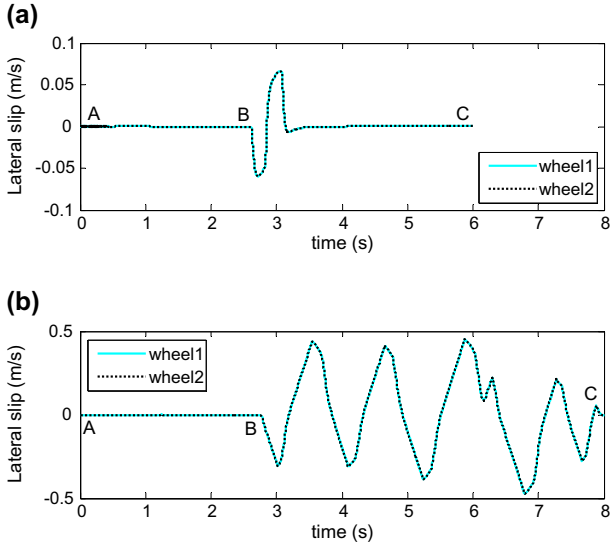

Figure 12. Lateral slip velocity on (a) Surface 1 and (b) Surface 2.

In this case, we show that by using the path-following controller with a dynamic planner developed in this paper, we can adaptively change the desired forward velocity based on the available traction force (which is a function of slip) and, thus, can stabilize the WMR during path-following navigation at high-speed. In particular, we have seen in *Case II* that the WMR becomes unstable on Surface 2 when the desired forward velocity is set at 3.2 m/s. The WMR autonomously adjusts its desired forward velocity based on the algorithm in the dynamic planner as discussed under the section 'Dynamic

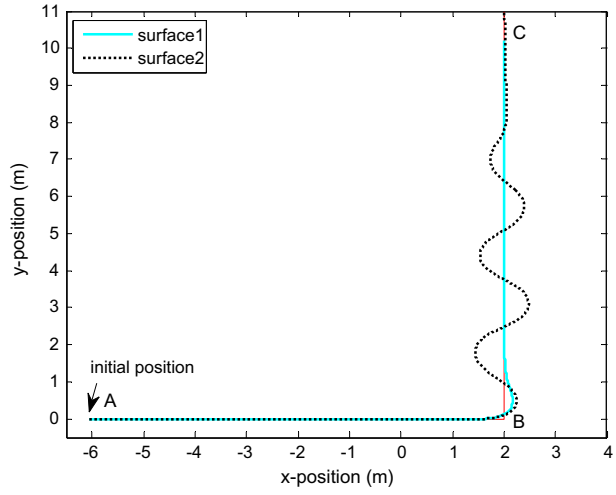

Figure 13. WMR's path-following trajectory.

Planner.' From Equations (31) and (32), the weighted coefficient is used to regulate the desired forward velocity. For example, when the WMR is at zero velocity, the lateral traction force is zero. This set $J(F)=0$ and $K(F)=1$, and the desired forward velocity becomes the maximum allowable forward velocity. If the WMR is at the maximum allowable traction, $J(F)$ becomes infinity and $K(F)=0$. This signals the robot to reduce its current forward velocity. The rate of regulation of forward velocity can be controlled by setting the decay factor, μ accordingly.

Here, we show that by dynamically changing the desired forward velocity during cornering, the WMR can be made to follow the path on Surface 2. Figure 13 shows that the WMR can take the sharp turn in a relatively stable manner with significant overshoot.

Figure 14 shows a comparison of the desired forward velocity profiles before after the dynamic planner is

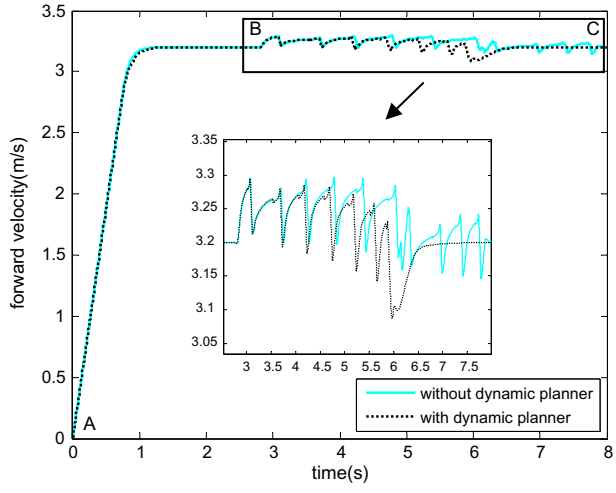

Figure 14. Forward velocity profile.

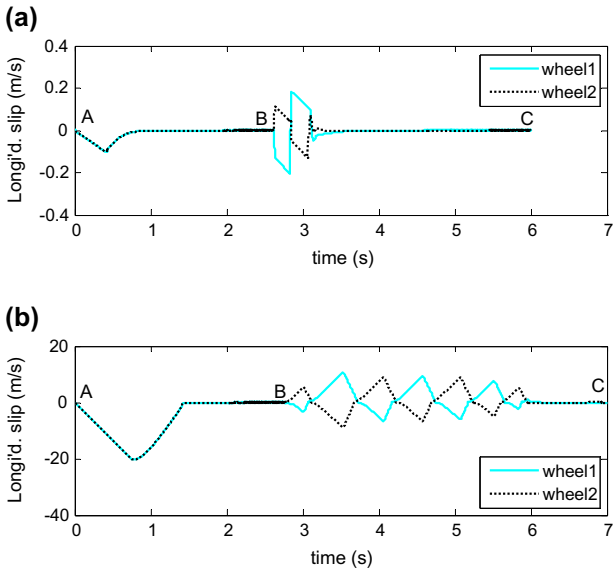

Figure 15. Longitudinal slip velocity on (a) Surface 1 and (b) Surface 2.

applied. It is clear that by using the dynamic path-following controller, the desired forward velocity is reduced in such a manner to make the navigation stable on Surface 2. In Figure 15, we also see that the longitudinal slip for wheel 1 on Surface 2 is getting stable as its magnitude is getting smaller over time on segment BC. The same feature that is the magnitude of lateral slip getting smaller is also reflected on lateral slip profile, as shown in Figure 16.

The above simulation results indicate that the presented modeling technique is able to capture slip phenomenon during WMR navigation. Furthermore, the

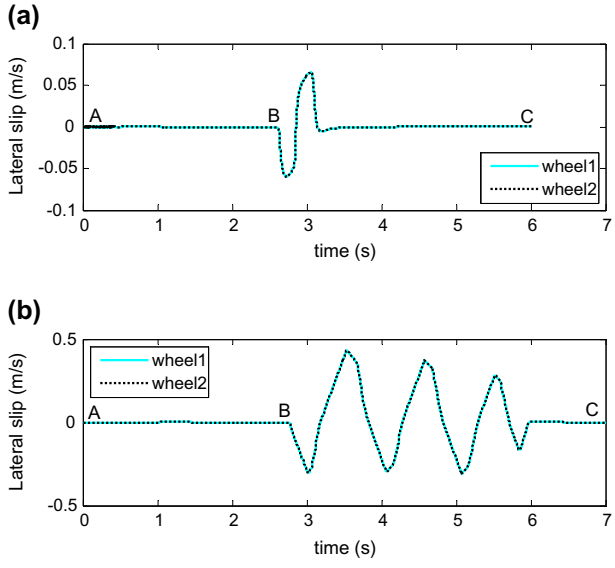

Figure 16. Lateral slip velocity on (a) Surface 1 and (b) Surface 2.

control and planning techniques allow for autonomous adjustment of cornering velocity based on traction properties of different surfaces such that the WMR can take turns without being unstable. Note that in these simulations, we assume that we can identify the surfaces and know their traction properties, and can measure slips. In real applications, in order to model slip and traction force in the dynamics, we need to measure the slip and identify the surface characteristics. Slip measurement and surface identification are separate research topics and are beyond the scope of this paper. In this paper, we assume that such information are available to us based on the works of other research groups that focus on slip measurement and surface identification. For the interested readers, some papers that discussed the surface identification using different techniques are [23,27–29]. Different ways of measuring wheel slip have been reported in [22,30–33]. In addition, [24,32,34] provided an excellent review of current trends in modeling the traction forces.

5. Conclusion

In this paper, we investigate how a WMR can navigate in the presence of slip. We model the WMR in such a way that the wheel and ground contact point allows slip. In order to include the slip dynamics into the WMR dynamics, we augment the generalized coordinates of the WMR by including the slip coordinates and develop an integrated dynamic model that can simulate WMR motion in the presence of slip. The presented dynamic model is a new contribution in the literature. Subsequently, we design a path-following controller and a dynamic planner for the WMR that can improve the performance of navigation and to avoid instability in the presence of slip. In particular, this control technique allows the WMR to exploit slip to improve maneuverability. Instead of suppressing slip or avoiding it by sacrificing the WMR velocity significantly during cornering, the presented approach exploits slip–traction properties to generate as much velocity as possible without causing instability of the WMR. As a result, such an approach has the potential to enhance WMR navigation performance in real-world situation when the tasks demand sudden changes in motion at high speeds. It will help the WMR to autonomously adjust its speed appropriately based on the environmental conditions and, thus, will help achieve smarter navigation capabilities in the future. We demonstrate by a series of simulation studies to illustrate the performance of the proposed modeling and control technique for the case where slip exists. The more realistic nature of the simulation with the inclusion of slip phenomenon should increase the efficacy of the controller developed for the WMR applications. We plan to implement the dynamic planner and the path-following controller into a *Pioneer P3DX* robot in order to validate the techniques in the near future.

Acknowledgments

The authors gratefully acknowledge ONR grant N00014-03-1-0052 and N00014-06-1-0146 that partially supported this work.

Notes on contributors

Naim Sidek received the PhD degree from Vanderbilt University, TN in electrical engineering in 2008. He is currently an assistant professor of mechatronics engineering at Department of Mechatronics Engineering, International Islamic University Malaysia. His research interests include human-centered electromechanical devices, soft computing, and control.

Nilanjan Sarkar received the PhD degree from University of Pennsylvania, Philadelphia, PA. in mechanical engineering and applied mechanics in 1993. He was an assistant professor at the University of Hawaii, Manoa, HI. He joined Vanderbilt University, Nashville, TN in 2000. He is currently a professor of mechanical engineering, and Computer Engineering in the Department of Mechanical Engineering and the Department of Electrical Engineering and Computer Science in Vanderbilt University. His research interests include human–robot interaction, affective computing, dynamics, and control.

References

[1] Peasgood M. A complete and scalable strategy for coordinating multiples robots within roadmaps. IEEE Trans. Robot. 2008;24:283–292.

[2] Eghtesad M, Necsulescu DS. Study of the internal dynamics of an autonomous mobile robot. Robot. Auton. Syst. 2006;54:342–349.

[3] Conceicao AS, Oliveira HP, Sousa e Silva A, Oliveira D, Moreira AP. A nonlinear model predictive control of an omni-directional mobile robot. In: IEEE International Symposium on Industrial Electronics; 2007 June. p. 2161–2166.

[4] Dongbin Z, Jianqiang Y, Xuyue D. Motion regulation of redundantly actuated omni-directional wheeled mobile robots with internal force control. In: IEEE/RSJ International Conference on Intelligent Robots and Systems; 2007. p. 3919–3924.

[5] Liyong Y, Wei X. An adaptive tracking method for nonholonomic wheeled mobile robots. In: Control Conference, 2007. CCC 2007. Chinese; 2007 Jun 26–31. p. 801–805.

[6] Salerno A, Angeles J. A new family of two-wheeled mobile robots: modeling and controllability. IEEE Trans. Robot. 2007;23:169–173.

[7] Motte I, Campion I. A slow manifold approach for the control of mobile robots not satisfying the kinematic constraints. IEEE Trans. Robot. Autom. 2000;16:875–880.

[8] Lin W-S, Chang L-H, Yang P-C. Adaptive critic anti-slip control of wheeled autonomous robot. IET Control Theory Appl. 2007;1:51–57.

[9] Tarokh M, McDermott GJ. Kinematics modeling and analyses of articulated rover. IEEE Trans. Robot. 2005;21: 539–553.

[10] Volpe R. Navigation results from desert field tests of the rocky 7 Mars rover prototype. Int. J. Robot. Res. 1999;18:669–683.

[11] Dixon WE, Dawson DM, Zergeroglu E. Robust control of a mobile robot system with kinematic disturbance. In: IEEE International Conference on Control Applications; 2000. p. 437–442.

[12] Balakrishna R, Ghosal A. Modeling of slip for wheeled mobile robot. IEEE Trans. Robot. Autom. 1995;11: 126–132.

[13] Jung S, Hsia TC. Explicit lateral tire force control of an autonomous mobile robot with slip. In: IEEE/RSJ International Conference on Intelligent Robots and Systems (IROS); 2005. p. 388–393.

[14] Stonier D, Hyoung C Se-, Sung-Lok C, Kuppuswamy NS, Jong-Hwan K. Nonlinear slip dynamics for an omniwheel mobile robot platform. In: IEEE International Conference on Robotics and Automation; 2007 April. p. 2367–2372.

[15] Mohammadpour E, Naraghi M. Robust adaptive stabilization of skid steer wheeled mobile robots considering slipping effects. Adv. Robot. 2011;25:205–227.

[16] Graciam L, Tornero J. Kinematic modeling of wheeled mobile robots with slip. Adv. Robot. 2007;21: 1253–1279.

[17] Ishigami G, Nagatani K,Yoshida K. Path planning for planetary exploration rovers and its evaluation based on wheel slip dynamics. In: Proceedings of IEEE International Conference on Robotics and Automation; 2007.

[18] Zhu X, Dong G, Hu D, Cai Z. Robust tracking control of wheeled mobile robots not satisfying nonholonomic constraints. In: the 6th International Conference on Intelligent Systems Design and Applications (ISDA'06); 2006.

[19] Kumar V, Wellman P, Krovi V. Adaptive mobility system, United States Patent 5,513,716. Appl. No.: 239,951. Filed: May 9, 1994, Granted: 1996 May 7.

[20] Sarkar N, Yun X. Control of mechanical systems with rolling constraints: application to the dynamic control of mobile robots. Int. J. Robot. Res. 1994;31:55–69.

[21] Yun X, Yamamoto Y. Internal dynamics of a wheeled mobile robot. In: IEEE/RSJ International Conference on Intelligent Robots and Systems. 1993, July 26–30; Yokohama, Japan. p. 1288–1294.

[22] Ward CC, Iagnemma K. Model-based wheel slip detection for outdoor mobile robots. In: IEEE International Conference on Robotics and Automation; 2007. p. 2724–2729.

[23] Politiz Z, Probert Smith PJ. Classification of textured surfaces for robot navigation using continuous transmission frequency-modulated sonar signatures. Int. J. Robot. Res. 2001;20:107–128.

[24] Li L, Wang FY. Integrated longitudinal and lateral tire/road friction modeling and monitoring for vehicle motion control. IEEE Trans. Intell. Transp. Syst. 2006;7:1–19.

[25] Muller S, Uchanski M, Hedrick K. Estimation of the maximum tire-road friction coefficient. J. Dyn. Syst. Meas. Control. 2003;1:607–617.

[26] Wang J, Alexander L, Rajamani R. GPS based real-time tire-road friction coefficient identification. Minnesota, USA: Minnesota Department of Transportation, Research Service Section; 2004.

[27] Brooks CA, Iagnemma K. Vibration-based terrain classification for planetary exploration rovers. IEEE Trans. Robot. Autom. 2005;21:1185–1191.

[28] Vandapel N, Huber DF, Kapuria A, Hebert M. Natural terrain classification using 3-D ladar data. In: Proceedings of IEEE International Conference on Robotics and Automation. Vol. 26; 2004. p. 5117–5122.

[29] Weiss C, Frohlich H, Zell A. Vibration-based terrain classification using support vector machines. In: IEEE/RSJ International Conference on Intelligent Robots and Systems; 2006. p. 4429–4434.

[30] Angelova A, Matthies L, Helmick DM, Sibley G, Perona P. Learning to predict slip for ground robots. In: Proceedings of IEEE International Conference on Robotics and Automation; 2006. p. 3324–3331.

[31] Helmick DM, Yang C, Clouse DS, Matthies LH, Roumeliotis SI. Path following using visual odometry for a Mars rover in high-slip environments. In: Proceedings IEEE Aerospace Conference. Vol. 2; 2004. p. 2772–789.

[32] Helmick DM, Yang C, Clouse DS, Bajracharya M, Matthies LH. 2005 Slip compensation for a Mars rover. In: IEEE/RSJ International Conference on Intelligent Robots and Systems (IROS); 2005. p. 2806–2813.

[33] Ray LR. Nonlinear tire force estimation and road friction identification: simulation and experiments. J. Autom. 1997;33:1819–1833.

[34] Baffet G, Charara A, Stephant J. Sideslip angle, lateral force and road friction estimation in simulations and experiments. In: Proceedings of IEEE International Conference on Control Applications; 2006. p. 903–908.